21. Verhagen, A. *et al.* Identification of DIABLO, a mammalian protein that promotes apoptosis by binding to and antagonizing IAP proteins. *Cell* **102,** 43–53 (2000).
22. Susin, S. A. *et al.* Molecular characterization of mitochondrial apoptosis-inducing factor. *Nature* **397,** 441–446 (1999).
23. Lindsten, T. *et al.* The combined functions of proapoptotic Bcl-2 family members Bak and Bax are essential for normal development of multiple tissues. *Mol. Cell* **6,** 1389–1399 (2000).
24. Kuida, K. *et al.* Decreased apoptosis in the brain and premature lethality in CPP32-deficient mice. *Nature* **384,** 368–372 (1996).
25. Hakem, R. *et al.* Differential requirement for caspase 9 in apoptotic pathways *in vivo*. *Cell* **94,** 339–352 (1998).
26. Kuida, K. *et al.* Reduced apoptosis and cytochrome c-mediated caspase activation in mice lacking caspase 9. *Cell* **94,** 325–337 (1998).
27. Cecconi, F. *et al.* Apaf1 (CED-4 homolog) regulates programmed cell death in mammalian development. *Cell* **94,** 727–737 (1998).
28. Yoshida, H. *et al.* Apaf1 is required for mitochondrial pathways of apoptosis and brain development. *Cell* **94,** 739–750 (1998).
29. Honarpour, N. *et al.* Adult Apaf-1-deficient mice exhibit male infertility. *Dev. Biol.* **218,** 248–258 (2000).
30. Chautan, M. *et al.* Interdigital cell death can occur through a necrotic and caspase-independent pathway. *Curr. Biol.* **9,** 967–970 (1999).

Supplementary information is available on *Nature*'s World-Wide Web site (http://www.nature.com) or as paper copy from the London editorial office of *Nature*.

Acknowledgements

We thank J. M. Peters, M. Lutter and M. Fang for their assistance in mitochondrion purification and other techniques; Y. Li and R. Harold for technical support; J. Zhang and M. Xu for providing DFF45-knockout MEF cells. We also thank M. Lutter and X. Jiang for recombinant Bcl-x_L. X.L. is supported by the Leukemia Society of America; X.W. is supported by grants from NIH and the Welch Foundation.

Correspondence and requests for materials should be addressed to X.W. (e-mail: xwang@biochem.swmed.edu).

corrections

Timing of the Last Glacial Maximum from observed sea-level minima

Yusuke Yokoyama, Kurt Lambeck, Patrick De Deckker, Paul Johnston & I. Keith Fifield

Nature **406,** 713–716 (2000).

In this Letter, a statement on page 715 that the eustatic sea level $\Delta\zeta_{eus}(t)$ differs from the ice-volume-equivalent sea level $\Delta\zeta_e(t)$ is erroneous. We thank W. R. Peltier for drawing this error in interpretation to our attention. The two definitions were initially introduced to distinguish changes in sea level that were the result of ice mass being added to the oceans from other changes caused by thermal expansion, for example. The erroneous statement was the result of a programming error that was introduced into the program in 1998 when it was modified to deal with shelf ice more accurately and to introduce the time dependence of the coastlines in the evaluation of the equivalent sea-level change through equation (3). This evaluation requires a knowledge of the location of the shoreline at each time step, of the grounding line of the ice and of the part of the shelf ice that floats or grounds as a result of sea level change and shelf-ice thickness change. The error was introduced at the end of each iteration of the sea-level equation, when the value of sea level change was integrated over the ocean and the resulting volume was compared with the change in ice volume for the corresponding interval. The eustatic sea level at this stage was defined as the global average of sea-level change but, because we allow sea level to be non-zero on land so as to be able to compute the tilting of lakes or the changing elevations of tree lines, the averaging should have been restricted to the ocean. Fortunately, the error does not enter into any other part of the model predictions because the estimate of global sea level rise is based on the ice volume change in equation (3) throughout the core program. Thus calculations of the isostatic correction $\Delta\zeta_i(j,t)$ in equation (1) and of the ice-volume-equivalent sea level $\Delta\zeta_e(t)$ are correct, as are the results illustrated in Fig. 2. The matter arises in the two sentences in parentheses of the penultimate paragraph of the main text (page 715), in a discussion of the difference between our Barbados results and those of Peltier. The first sentence in parentheses remains correct, but our attempt to explain it in the second sentence is not. The cause for the disagreement must be sought elsewhere, possibly in the different ice and/or earth models used. □

The role of interleukin-1 polymorphisms in the pathogenesis of gastric cancer

Emad M. El-Omar, Mary Carrington, Wong-Ho Chow, Kenneth E. L. McColl, Jay H. Bream, Howard A. Young, Jesus Herrera, Jolanta Lissowska, Chiu-Chin Yuan, Nathaniel Rothman, George Lanyon, Maureen Martin, Joseph F. Fraumeni Jr & Charles S. Rabkin

Nature **404,** 398–402 (2000).

We reported the association of interleukin-1 gene cluster polymorphisms suspected of enhancing production of interleukin-1 β with an increased risk both of hypochlorhydria induced by *Helicobacter pylori* and of gastric cancer. We were subsequently alerted to an error in our genotyping by a report[1] that the *IL-1B*-511T variant is in positive linkage disequilibrium with the *IL-1B*-31C allele, rather than with the *IL-1B*-31T allele as we had stated. We have traced this discrepancy to incorrect labelling of the sequence data from the wild-type and variant controls for the *IL-1B*-31 assays. Consequently, the designations *IL-1B*-31T and *IL-1B*-31C were reversed in the text and Tables 1–3. We have now verified the proper identifications by re-sequencing our controls. In addition, we have confirmed the more common (*IL-1B*-31T/*IL-1B*-511C) and less common (*IL-1B*-31C/*IL-1B*-511T) haplotypes by forward and reverse sequencing five homozygous samples (two wild-type and three variant) for both of these loci. Our data and analysis remain otherwise unchanged. The electrophoretic mobility shift assays were unaffected by this error and hence the greater DNA binding of the *IL-1B*-31T-bearing oligonucleotide represents the wild-type *IL-1B* promoter. □

1. Hamajima, N. *et al.* Interleukin-1 polymorphisms, lifestyle factors, and *Helicobacter pylori* infection. *Jpn J. Cancer Res.* **92,** 383–389 (2001).

16. Brunink, J. A. J. *et al.* The application of metalloporphyrins as coating material for quartz microbalance-based chemical sensors. *Anal. Chim. Acta* **325,** 53–64 (1996).
17. Di Natale, C. *et al.* The exploitation of metalloporphyrins as chemically interactive material in chemical sensors. *Mater. Sci. Eng. C* **5,** 209–215 (1998).
18. Blauer, G. & Sund, H. (eds) *Optical Properties and Structure of Tetrapyrroles* (de Gruyter, Berlin, 1985).
19. Nappa, M. & Valentine, J. S. The influence of axial ligands on metalloporphyrin visible absorption spectra. Complexes of tetraphenylporphinatozinc. *J. Am. Chem. Soc.* **100,** 5075–5080 (1978).
20. Suslick, K. S. & Van Deusen-Jeffries, S. in *Comprehensive Supramolecular Chemistry* (ed. Lehn, J. M.) 141–170 (Elsevier, Oxford, 1996).
21. Bhyrappa, P., Young, J. K., Moore, J. S. & Suslick, K. S. Dendrimer porphyrins: synthesis and catalysis. *J. Am. Chem. Soc.* **118,** 5708–5711 (1996).
22. Chou, J.-H., Nalwa, H. S., Kosal, M. E., Rakow, N. A. & Suslick, K. S. in *The Porphyrin Handbook* (eds Kadish, K., Smith, K. & Guilard, R.) 43–132 (Academic, New York, 2000).
23. Bhyrappa, P., Vaijayanthimala, G. & Suslick, K. S. Shape-selective ligation to dendrimer-metallo-porphyrins. *J. Am. Chem. Soc.* **121,** 262–263 (1999).
24. Sen, A. & Suslick, K. S. Shape selective discrimination of small organic molecules. *J. Am. Chem. Soc.* (in the press).
25. Adler, A. D. *et al.* A simplified synthesis for meso-tetraphenylporphin. *J. Org. Chem.* **32,** 476 (1967).
26. Adler, A. D., Longo, F. R., Kampas, F. & Kim, J. On the preparation of metalloporphyrins. *J. Inorg. Nucl. Chem.* **32,** 2443–2445 (1970).
27. Barley, M., Becker, J. Y., Domazetis, G., Dolphin, D. & James, B. R. Synthesis and redox chemistry of octaethylporphyrin complexes of ruthenium(II) and ruthenium(III). *Can. J. Chem.* **61,** 2389–2396 (1983).
28. Datta-Gupta, N. & Bardos, T. J. Synthetic porphyrins II: preparation and spectra of some metal chelates of para-substituted-meso-tetraphenylporphines. *J. Pharm. Sci.* **57,** 300–304 (1968).
29. Yaws, C. L. *Handbook of Vapor Pressure* (Gulf, Houston, 1994).

Supplementary Information is available on *Nature*'s World-Wide Web site (http://www.nature.com) or as paper copy from the London editorial office of *Nature*.

Acknowledgements

This work was supported by the US NIH and in part by the US DOD and DOE.

Correspondence and requests for materials should be addressed to K.S.S. (e-mail: ksuslick@uiuc.edu).

Timing of the Last Glacial Maximum from observed sea-level minima

Yusuke Yokoyama*†, Kurt Lambeck*, Patrick De Deckker‡, Paul Johnston* & L. Keith Fifield§

* *Research School of Earth Sciences,* ‡ *Department of Geology,* § *Department of Nuclear Physics, Research School of Physical Sciences and Engineering, The Australian National University, Canberra, ACT 0200, Australia*

During the Last Glacial Maximum, ice sheets covered large areas in northern latitudes and global temperatures were significantly lower than today. But few direct estimates exist of the volume of the ice sheets, or the timing and rates of change during their advance and retreat[1,2]. Here we analyse four distinct sediment facies in the shallow, tectonically stable Bonaparte Gulf, Australia—each of which is characteristic of a distinct range in sea level—to estimate the maximum volume of land-based ice during the last glaciation and the timing of the initial melting phase. We use faunal assemblages and preservation status of the sediments to distinguish open marine, shallow marine, marginal marine and brackish conditions, and estimate the timing and the mass of the ice sheets using radiocarbon dating and glacio-hydro-isostatic modelling. Our results indicate that from at least 22,000 to 19,000 (calendar) years before present, land-based ice volume was at its maximum, exceeding today's grounded ice sheets by 52.5×10^6 km^3. A rapid decrease in ice volume by about 10% within a few hundred years terminated the Last Glacial Maximum at 19,000 ± 250 years.

† Present address: Space Sciences Laboratory, University of California, Berkeley, California, USA, and Lawrence Livermore National Laboratory, 7000 East Avenue, PO Box 808, L-202 Livermore, California 94550, USA.

The broad and shallow continental margin of northern Australia includes several local bathymetric depressions, the largest of which is the Bonaparte Gulf. During times of sea-level lowstands much of the shelf was exposed, and the sediments deposited in the depressions were protected from wave action by the outer shelf edge. A total of 23 gravity cores, 10 vibrocores and 3 grab samples were collected from present-day water depths of 34 to 147 m along transects across the shelf margin and the Bonaparte depression (Fig. 1a). All cores were sedimentologically examined and a number were selected for micro-palaeontological analysis and radiocarbon dating. Depending on faunal assemblages and preservation status (Fig. 1b, see also Methods section below) four distinct bio-sedimentary facies have been recognized: open marine, shallow marine, marginal marine, and brackish water, denoted by OM, SM, MM and BR, respectively, in Fig. 1b. We obtained 41 radiocarbon dates of foraminifera and bivalve molluscs using accelerator mass spectrometry (AMS) techniques and dated some of the larger bivalves using conventional liquid scintillation counting methods. All AMS-dated samples were severely etched (about 40% to 50%) to discard outer shell material that may have been contaminated by secondary carbonate precipitation. Figure 1b summarizes the results for 7 of the cores from water depths between 128 and 95 m. All carbonate ages have been corrected for reservoir effect (400 years; refs 3, 4) and calibrated to a calendar timescale[5,6]. The cores indicate excellent preservation of faunal specimens, many without evidence for reworking, and the ^{14}C dates indicate only rare instances of age inversions.

Last Glacial Maximum (LGM) sea-level indicators are preserved in a number of the cores. To reconstruct a sea-level curve based on micropalaeontological evidence, it is necessary to consider the palaeoenvironmental conditions as a sequence of events assuming that little or no break in sedimentation, and no erosion, has occurred. (If a hiatus does occur it results in missing bio-facies and in reworking of the faunas; and this is not observed.) Thus, through identification of a transition from shallow marginal marine to brackish conditions and then back to shallow marginal marine conditions, the timing of the brackish conditions records the interval of lowest sea level. Once this depth is identified in a single core, other cores with depths either side of the identified low sea-level stand are examined to substantiate the reconstruction. This has been done using core GC5 as the master core because it has the best preserved and dated record for brackish water conditions. No truly lacustrine phase has been recognised in any of the cores, indicating that throughout the LGM the Bonaparte depression remained in open contact with the Timor Sea[7].

The transition from marginal marine to brackish facies occurs in core GC5 at 21,280 calendar years before present (cal. yr BP) at a depth of 340 cm below the sea floor (Fig. 1b). Sediments below this depth contain marine ostracods and planktonic foraminifers, whereas above this boundary dwarf specimens of the benthic foraminifer *Ammonia beccarii* occur along with other shallow to brackish water indicators such as the benthic foraminifer *Elphidium* spp. and the euryhaline ostracod *Cyprideis australiensis*[8,9]. Marginal marine and brackish-water conditions existed for about 3,000 years, in agreement with results from cores GC4 and GC6 (Fig. 1b) as well as GB1. Sea level at GC5 was, therefore, a few metres below −121 m (Fig. 2a) in this time interval. Deeper cores, both within the depression (GC1, GC2 and GC3) and outside it, do not indicate any brackish facies and place a lower limit of −125 m on the position of relative sea-level at these locations. The microfossil assemblages of cores GC10 and GC11, at −103 and −101 m respectively, are indicative of a marginal beach or coastal lagoon environment between 17,650 and 17,450 cal. yr BP. In core GC7, undamaged littoral-dwelling bivalves occur at −107 m with an age of 17,610 cal. yr BP (Fig. 1b). Figure 2a illustrates the results for all samples free from post-depositional disturbance. They indicate that between 22,000 and 19,000 cal. yr BP a rapid rise of 10–15 m occurred.

The sea-level change due to the melting of land-based ice sheets is[10,11]

$$\Delta\zeta_{rsl} = \Delta\zeta_e + \Delta\zeta_i \quad (1)$$

where

$$\Delta\zeta_e(t) = -\frac{\rho_i}{\rho_w}\int_t \frac{1}{A_w(t)}\frac{dV_i}{dt}dt \quad (2)$$

is a measure of the ice volume V_i that contributed to the sea-level rise. We call this the ice-equivalent sea-level change. A_w is the ocean area and ρ_i, ρ_w are the average densities of ice and ocean, respectively. $\Delta\zeta_i$ is the total glacio-hydro-isostatic contribution to sea-level change. At the Australian sites, away from the former ice sheets, the isostatic response is one of subsidence of the sea floor and coastal zone because of the meltwater loading of the ocean floor. Here, $\Delta\zeta_i$ is

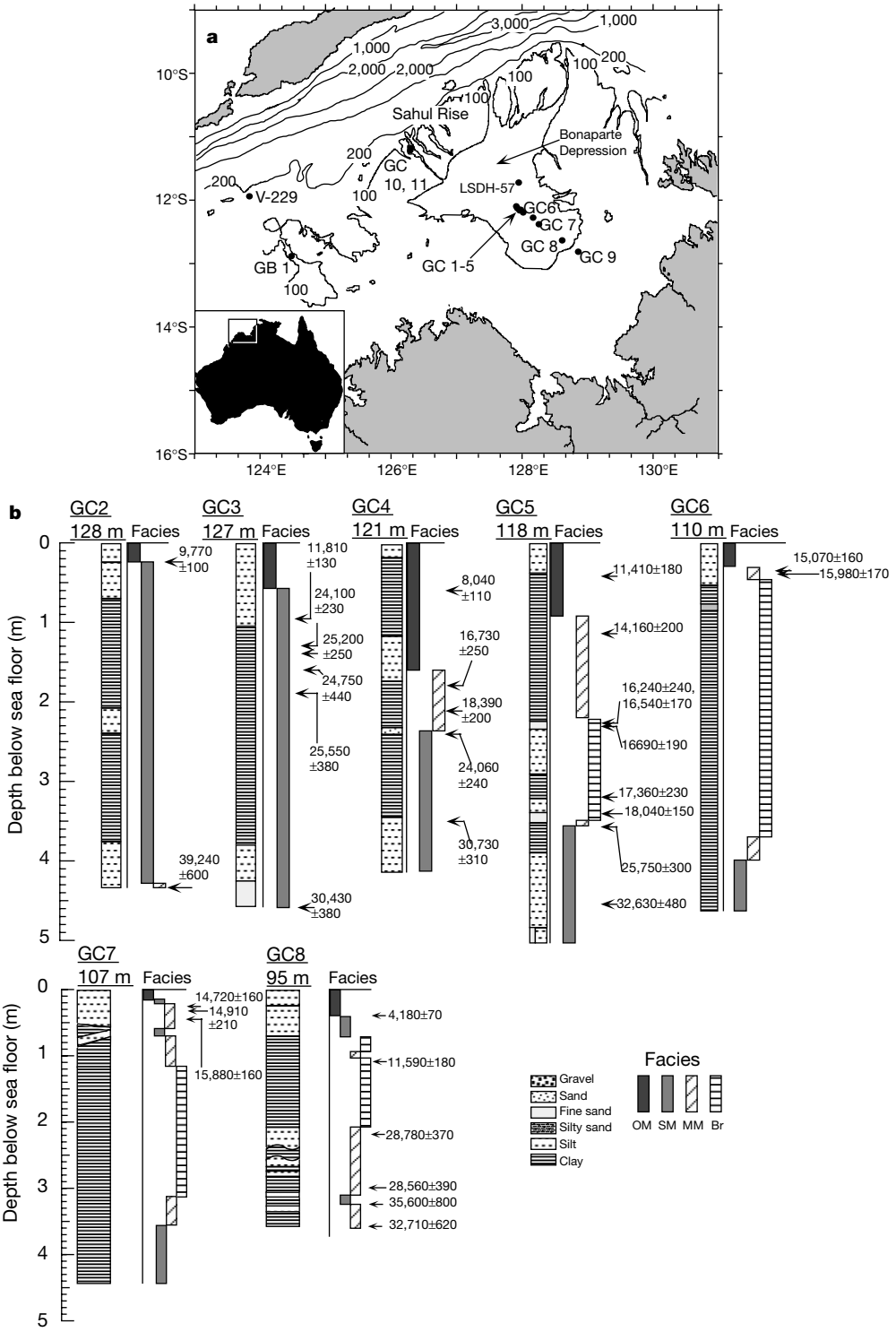

Figure 1 Location and stratigraphy of the Bonaparte cores. **a**, Location of the sampling sites on the northwest shelf of Australia with bathymetric contours (in metres) and coring sites. **b**, Sedimentological description with facies inferred from micro-palaeontological methods (see Methods) and ^{14}C dates for gravity cores. Four facies are identified as follows: OM, open marine; SM, shallow marine; MM, marginal marine; and BR, brackish-water (see Methods section). Dated horizons are indicated and all ages are in ^{14}C years. The complete data set, including calibrated ages, is available from http://www.ngdc.noaa.gov/paleo/data.html.

about 10% of the primary contribution $\Delta\zeta_e$ and the relative sea levels lie above the ice-equivalent sea level at the time of the LGM[12].

The isostatic effects also need to be considered when estimating ice volumes from eustatic sea level $\Delta\zeta_{eus}$, defined as the globally averaged sea-level change. The value of $\Delta\zeta_i$ in equation (1) averaged over the oceans, $\langle\Delta\zeta_i\rangle_{Aw}$, at any time is non-zero because of the change in shape and depth of the ocean basin under the changing surface ice and water load. Hence the spatially averaged change in sea level at any time is $\Delta\zeta_{eus} = \Delta\zeta_e + \langle\Delta\zeta_i\rangle_{Aw}$ and the last term contributes about 20% to $\Delta\zeta_{eus}$. In addition to the time dependence of the depth of the ocean basin, the evaluation of the isostatic term in equation (1) and the integral in equation (2) includes the time dependence of both the coastline and the area of shallow sea floor covered by grounded ice.

Figure 2b illustrates the ice-equivalent sea level and associated land-based ice volume, inferred from the Bonaparte Gulf observations. These results use a rigorous glacio-hydro-isostatic formulation with Northern Hemisphere ice models that are consistent with observational evidence from these localities and with an Antarctic ice model that contributes 25 m to $\Delta\zeta_e$ (refs 13–15). Earth model parameters used in these corrections are based on analysis of Australian postglacial sea levels[12] and uncertainties in these parameters are included in evaluating the error bars of Fig. 2b. Because the isostatic corrections are about 10% of the total sea-level change, uncertainties in the distribution of ice between the different centres of glaciation contribute little to the magnitude of the isostatic effects

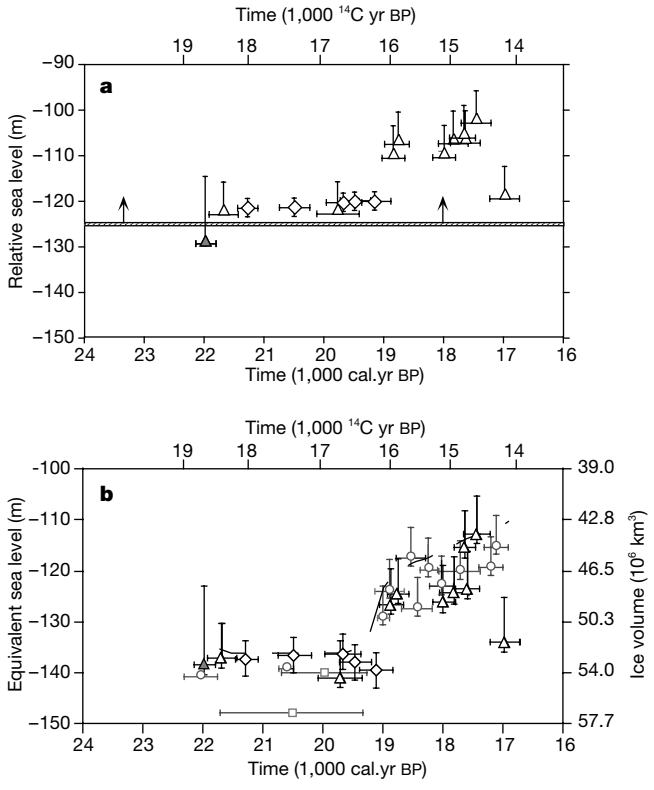

Figure 2 Sea level and ice volumes during the LGM. **a**, Observed sea level for the Bonaparte depression. The diamonds correspond to brackish-water facies, the triangles to marginal marine facies and the filed triangle to shallow marine facies. The hatched zone corresponds to the lower-limit estimate for relative sea level (according to results obtained from GC2 and 3 that neither core contains the shallow-water facies). **b**, Equivalent sea-level and ice-volume estimates. The circles correspond to the isostatically corrected Barbados data[19,20], and the squares correspond to earlier estimates for the Northwest Shelf[7]. The diamonds correspond again to brackish-water facies, the triangles to marginal marine facies, and the filled triangle to shallow marine facies. The dashed line defines the ice-equivalent sea-level function. Age uncertainties correspond to 1σ except for U/Th dated Barbados corals (2σ level)[20].

themselves. The consequence of the isostatic corrections is that the ice-volume-equivalent sea level at the LGM lies between −135 and −130 m, corresponding to a volume of grounded ice in excess of the present volume by $(52 \pm 2) \times 10^6$ km^3.

Earlier observations of the LGM sea level on the Australian shelf[7,16] and elsewhere[17,18] have shown considerable uncertainty, in part because of the limitation of the preserved indicators and in part because of inadequate age determination. Of the previous data, that of greatest importance is the Barbados evidence where the depth–age relationship of corals have placed lower limits on the local sea-level curve[19,20]. Figure 2b includes isostatically corrected sea-level estimates—using the same model and model parameters as for the Bonaparte data—for the Barbados data as well as three earlier estimates from northern Australia[7]. The main group of Barbados results, from *Acropora* corals that live in water depths down to about 5 m (ref. 19), occur in the interval from 19,000 to 17,000 cal. yr BP and, when corrected for the differential isostatic effects, are consistent with the Bonaparte Gulf data. The two older data points from Barbados lie at greater depths and are also consistent with the new data for the corresponding period. The agreement between the Barbados and Bonaparte estimates shortly after 19,000 cal. yr BP indicate that the equivalent sea level stood at about −120 m at this time, above the coral and marginal marine samples. The earlier brackish water samples occur at about −135 m equivalent sea level. These estimates are from minimally reworked fauna showing evidence of bleaching and without age inversions. Thus a rapid rise in sea level occurred at about 19,000 cal. yr BP, within a time interval defined by the dating accuracy of a few hundred years. This rapid rise was followed by a period of about 2,000 to 3,000 years of much slower melting of the ice sheets before the onset of the main phase of late-glacial melting. The bulk of the Barbados evidence, therefore, does not correspond to the period of maximum glaciation but to the early stages of the late-glacial phase.

The inferred ice-equivalent sea level of −130 to −135 m is consistent with the glaciological lower limit estimate of −127 m established by the CLIMAP project[1] and does not support the maximum CLIMAP ice-sheet reconstruction of −163 m. (It has been argued that upper- and lower-limit CLIMAP models contain excessive ice when compared with an isostatically corrected Barbados sea-level result of −105 m (ref. 21). But this latter quantity corresponds to $\Delta\zeta_{eus}$, not $\Delta\zeta_e$. A $\Delta\zeta_{eus}$ of −105 m corresponds in fact to $\Delta\zeta$ of about −135 m.)

The global sea-level observations do not indicate where the ice was stored. Analyses of sea-level data from formerly glaciated regions provide Northern Hemisphere ice volumes that are less than those contained in glaciologically based models[13,21–23] and the previously noted[14,24] discrepancy between the Northern Hemisphere and total LGM ice volumes remains. Changes in Antarctic ice may account for part of this, although estimates based on Antarctic rebound analyses are inadequate to explain the entire imbalance[25]. In the inversion of sea-level data it is the rebound within the former ice margins that is most sensitive to changes in ice volume, but the necessary observations occur only once the area becomes ice free. Hence, ice volumes for the LGM and early part of the late-glacial period remain poorly constrained in such analyses[26]. The rapid rise in sea level noted at 19,000 cal. yr BP may provide part of the answer to the missing-ice problem: that the LGM ice sheets were initially cold-based, steeply domed and thick but then, in response to basal thawing over some regions, evolved rapidly into relatively thin ice cover with a significant reduction in ice volume[27,28]. Such a hypothesis is consistent with the geomorphological field evidence[27], with glaciological modelling[29] and with the ice models inferred from rebound analyses[13,22]. □

Methods

Facies determination

To define water depth within 1–2 m in the Bonaparte Gulf, it is necessary to examine the sequence of depositional events immediately before and after the deposition of the

brackish facies. In a falling sea-level sequence the following biosedimentological facies sequence can be expected within the core: 1, open marine; 2, shallow marine; 3, marginal marine; and 4, brackish conditions. The last three facies are seen, for example, in the lower part of core 5 (Fig. 1b). When sea level rises the sequence reverts to marginal marine and then to shallow marine. It is this sequence of facies changes before and after the deposition of the brackish-water sediments that determine the position and duration of shallow-water conditions. The four depositional sequences are as follows.

"Open marine" was identified by the presence of fragile pteropod remains, numerous and diversified benthic foraminifer and ostracod taxa, that are indicative of normal marine salinity. In analogy with modern conditions, water depths are around 20 m because planktonic foraminifers are either absent or rare.

"Shallow marine" was characterized by the absence of pteropods and the presence of numerous and well-preserved foraminifer and ostracod taxa (which include species of *Aglaiella*, *Argilloecia*, *Callistocythere*, *Loxoconcha*, *Pterygocythereis*, *Ulocleberis*, in addition to common bairdiid taxa); there are no planktonic foraminifers. Biodiversity of the microbiota is substantially lower than in the open marine facies. Water depths are around 10 m.

"Marginal marine" was defined by a change to a lower diversity of benthic marine ostracods (commonly encountered species: *Neocytheretta* ssp., *Xestoleberis* sp.) and benthic foraminifers, accompanied by the robust endobenthic scaphopods. Most specimens show signs of abrasion. Bivalve molluscs are common and frequently damaged. Broken echinoid spines and bryozoan remains are ubiquitous. Terrigenous material, mostly quartz, is common. Water depths are less than 5 m, being within the zone of tidal influence.

"Brackish water" was identified by a paucity of typically marine organisms and the presence of the foraminifer *Ammonia beccarii*, often in large numbers—and as dwarf morphs due to environmental stresses such as fluctuating salinities and temperatures—accompanied by the euryhaline ostracods *Cypridieis australiensis*, *Leptocythere* spp. and *Neocytheretta* spp. Signs of bleaching of the calcareous shells, indicating exposure to corrosive waters, are common. Terrigenous material is common. Salinities are well below sea-water salinity due to a strong influence of continental waters, such as found in estuaries and tidal flats. Water depths correspond to near mean sea level and up to the high-tide level. Present tidal range is ±3 m and this represents the upper limit of the accuracy of these sea-level indicators.

Received 23 July 1999; accepted 16 June 2000.

1. CLIMAP Project Members. Seasonal reconstructions of the earth's surface at the Last Glacial Maximum. *Geol. Soc. Am. Map Chart Ser.* **MC-36,** 1–18 (1981).
2. Bard, E. Ice age temperatures and geochemistry. *Science* **284,** 1133–1134 (1999).
3. Stuiver, M. & Braziunas, T. F. Modeling atmospheric ^{14}C ages of marine samples to 10,000 BC. *Radiocarbon* **35,** 137–189 (1993).
4. Edwards, R. L. *et al.* A large drop in atmospheric $^{14}C/^{12}C$ and reduced melting in the Younger Dryas, documented with ^{230}Th ages of corals. *Science* **260,** 962–968 (1993).
5. Stuiver, M. & Reimer, P. J. Extended ^{14}C data base and revised CALIB 3.0 ^{14}C age calibration program. *Radiocarbon* **35,** 215–230 (1993).
6. Bard, E., Arnold, M., Hamelin, B., Tisnerat-Laborde, N. & Cabioch, G. Radiocarbon calibration by means of mass spectrometric $^{230}Th/^{234}U$ and ^{14}C ages of corals. An updated data base including samples from Barbados, Mururoa, and Tahiti. *Radiocarbon* **40,** 1085–1092 (1998).
7. van Andel, T. H., Heath, G. R., Moore, T. C. & McGeary, D. F. R. Late Quaternary history, climate, and oceanography of the Timor sea, Northwestern Australia. *Am. J. Sci.* **265,** 737–758 (1967).
8. De Decker, P. An account of the techniques using ostracods in palaeolimnology in Australia. *Palaeogeogr. Palaeoclimat. Palaeoecol.* **62,** 463–475 (1988).
9. Yassini, I. & Jones, B. G. (eds) *Recent Foraminifera and Ostracoda from Estuarine and Shelf Environments on the Southeastern Coast of Australia* (Univ. Wollongong Press, 1995).
10. Farrell, W. E. & Clark, J. A. On postglacial sealevel. *Geophys. J.* **46,** 79–116 (1976).
11. Nakada, M. & Lambeck, K. Glacial rebound and relative sea-level variations: a new appraisal. *Geophys. J. R. Astron. Soc.* **90,** 171–224 (1987).
12. Lambeck, K. & Nakada, M. Late Pleistocene and Holocene sea-level change along the Australian coast. *Palaeoceogr. Palaeoclimatol. Palaeoecol.* **89,** 143–176 (1990).
13. Lambeck, K., Smith, C. & Johnston, P. Sea-level change, glacial rebound and mantle viscosity for northern Europe. *Geophys. J. Int.* **134,** 102–144 (1998).
14. Nakada, M. & Lambeck, K. The melting history of the Late Pleistocene Antarctic ice sheet. *Nature* **33,** 36–40 (1988).
15. Fleming, K. *et al.* Refining the eustatic sea-level curve since the Last Glacial Maximum using far- and intermediate-field sites. *Earth Planet. Sci. Lett.* **163,** 327–342 (1998).
16. Ferland, M. A., Roy, P. S. & Murray–Wallace, C. V. Glacial lowstand deposits on the outer continental shelf of southeastern Australia. *Quat. Res.* **44,** 294–299 (1995).
17. Ota, Y., Matsushima, Y. & Moriwaki, H. Notes on the Holocene sea-level study in Japan. *Quat. Res. Jpn* **21,** 133–143 (1982).
18. Colonna, M., Casanova, J., Dullo, W.-C. & Camoin, G. Sea-level changes and $\delta^{18}O$ record for the past 34,000 yr from Mayotte Reef, Indian Ocean. *Quat. Res.* **46,** 335–339 (1996).
19. Fairbanks, R. G. A 17,000-year glacio-eustatic sea level record: influence of glacial melting rates on the Younger Dryas event and deep-ocean circulation. *Nature* **342,** 637–642 (1989).
20. Bard, E., Hamelin, B. & Fairbanks, R. G. UpTh ages obtained by mass spectrometry in corals from Barbados: sea level during the past 130,000 years. *Nature* **346,** 456–458 (1990).
21. Peltier, W. R. Ice age paleotopography. *Science* **265,** 195–201 (1994).
22. Tushingham, A. M. & Peltier, R. W. Ice-3G: A new global model of late Pleistocene deglaciation based upon geophysical predictions of post-glacial relative sea level change. *J. Geophys. Res.* **96,** 4497–4523 (1991).
23. Lambeck, K. Limits on the areal extent of the Barents Sea ice sheet in Late Weichselian time. *Glob. Planet. Change* **12,** 41–51 (1996).
24. Andrews, J. T. A case of missing water. *Nature* **358,** 281 (1992).
25. Zwartz, D., Lambeck, K., Bird, M. & Stone, J. in *The Antarctic Region: Geological Evolution and Processes* (ed. Ricci, C. A.) 821–828 (Terra Antarctica, Siena, 1997).
26. Johnston, P. & Lambeck, K. Automatic inference of ice models from postglacial sea-level observations: Theory and application to the British Isles. *J. Geophys. Res.* 13179–13194 (2000).
27. Kleman, J. & Hättestrand, C. Frozen-bed Fennoscandian and Laurentide ice sheets during the Last Glacial Maximum. *Nature* **402,** 63–66 (1999).
28. Clark, P. U., Alley, R. B. & Pollard, D. Northern hemisphere ice-sheet influences on global climate change. *Science* **286,** 1104–1111 (1999).
29. Licciardi, J. M., Clark, P. U., Jenson, J. W. & Macayeal, D. R. Deglaciation of a soft-bedded Laurentide ice sheet. *Quat. Sci. Rev.* **17,** 427–448 (1998).

Acknowledgements

We thank J. Marshall for providing access to cores collected by the Australian Geological Survey Organisation.

Correspondence and requests for materials should be addressed to K.L. (e-mail: Kurt.Lambeck@anu.edu.au).

Cursoriality in bipedal archosaurs

Terry D. Jones*†, James O. Farlow‡, John A. Ruben*, Donald M. Henderson§ & Willem J. Hillenius‖

* *Zoology Department, Oregon State University, Corvallis, Oregon 97331, USA*
‡ *Department of Geosciences, Indiana-Purdue University, Fort Wayne, Indiana 46805, USA*
§ *Department of Cell Biology and Anatomy, School of Medicine, The Johns Hopkins University, Baltimore, Maryland 21205, USA*
‖ *Biology Department, College of Charleston, Charleston, South Carolina 29424, USA*

Modern birds have markedly foreshortened tails and their body mass is centred anteriorly, near the wings[1–5]. To provide stability during powered flight, the avian centre of mass is far from the pelvis, which poses potential balance problems for cursorial birds. To compensate, avians adapted to running maintain the femur subhorizontally, with its distal end situated anteriorly, close to the animal's centre of mass; stride generation stems largely from parasagittal rotation of the lower leg about the knee joint[6–12]. In contrast, bipedal dinosaurs had a centre of mass near the hip joint and rotated the entire hindlimb during stride generation[4–8,11–13]. Here we show that these contrasting styles of cursoriality are tightly linked to longer relative total hindlimb length in cursorial birds than in bipedal dinosaurs. Surprisingly, *Caudipteryx*, described as a theropod dinosaur[14,15], possessed an anterior centre of mass and hindlimb proportions resembling those of cursorial birds. Accordingly, *Caudipteryx* probably used a running mechanism more similar to that of modern cursorial birds than to that of all other bipedal dinosaurs. These observations provide valuable clues about cursoriality in *Caudipteryx*, but may also have implications for interpreting the locomotory status of its ancestors.

In contrast to bipedal dinosaurs, the femur in cursorial birds contributes little to generation of stride length, and avian hindlimb movement is largely the result of retraction of the lower leg[7–12]. Hence, it might be expected that relative stride length in cursorial birds would be lower than that in bipedal dinosaurs. However, this is probably not the case—lengths of 'effective hindlimb' segments in birds (tibiotarsus + tarsometarsus) and dinosaurs (femur + tibia + metatarsal III) are equivalent[16] (Fig. 1a). Consequently, total hindlimb length in cursorial birds is invariably one-and-a-half times longer than in theropod and ornithopod dinosaurs (Fig. 1b). Additionally, as adept avian runners have evolved repeatedly from flighted ancestors[17], we conclude that these profound anatomical modifications that facilitate avian cursoriality are multiple convergent responses to secondary resumption of cursoriality in distantly related taxa independently derived from flighted ancestors.

† Present address: Department of Biology, Stephen F. Austin State University, Nachogdoches, Texas 75962, USA.

genotypes: (1) *elav*–GAL4/+; *UAS–wild-type* α-*synuclein*/+; (2) *UAS–A30P* α-*synuclein*/*elav*–GAL4; and (3) *UAS–A53T* α-*synuclein*/*elav*–GAL4. Sections were stained with haematoxylin and eosin. Time points monitored were 1, 10, 30 and 60 days. In addition, serial 1-μm sections of glutaraldehyde-fixed heads from flies of the same genotypes prepared at 1, 30 and 60 days were stained with toluidine blue to highlight degenerating cells. No evidence of excess neurodegeneration was detected using either technique.

To evaluate dopaminergic cells of the dorsomedial cluster by tyrosine hydroxylase immunostaining, serial 4-μm sections were cut to include the entire brain. Immunopositive cells at the level of the giant interneuron commissure, posterior to the fan-shaped body, were counted in well oriented frontal sections at 1, 10, 30 and 60 days. At 1 day all control and experimental sections contained four or five cells in the delineated region. At 30 and 60 days all controls showed four or five cells. At 30 and 60 days all α-synuclein-expressing animals (α-synuclein, *elav*–GAL4 and α-synuclein, *Ddc*–GAL4 transheterozygotes) showed 0 or 1 tyrosine-hydroxylase-positive cell in the defined region. Tyrosine-hydroxylase-positive cells outside the dorsomedial cluster were present, and served as internal controls for the immunostaining procedure. At least four, and usually between six and ten brains were examined for wild-type α-synuclein and each mutant α-synuclein. Controls included young and aged flies of the genotypes *elav*–GAL4/+ and *Ddc*–GAL4/+. We evaluated expression of α-synuclein and β-galactosidase on similar serial section preparations. Quantification was simplified in these experiments because no clear cell-body-associated α-synuclein or β-galactosidase immunoreactivity was observed in the aged α-synuclein transgenic flies at the times reported.

For histological examination of retinas, heads were fixed in glutaraldehyde and embedded in epon. Tangential retinal sections were prepared at a thickness of 1 μm and stained with toluidine blue (Fig 4).

Standard electron microscopy was performed on brains from 25-day-old experimental (*UAS–A30P* α-*synuclein*/*elav*–GAL4) and control (*elav*–GAL4/+) flies. For immunoelectron microscopy, pre-embedding immunohistochemistry with an Hrp-congugated secondary antibody was performed on 60-day adult brains from experimental (*UAS–A30P* α-*synuclein*/*elav*–GAL4) and control (*elav*–GAL4/+) flies fixed in 4% paraformaldehyde with 0.5% glutaraldehyde. Tissue was post-fixed in osmium and embedded in epon. Unstained ultrathin sections and ultrathin sections stained with uranyl acetate and lead citrate were examined.

Climbing assay

The climbing assay was performed as described[19,20]. Forty flies were placed in a plastic vial, and gently tapped to the bottom of the vial. The number of flies at the top of the vial was counted after 18 s of climbing. Twenty trials were performed for each time point. The data shown represent results from a cohort of flies tested serially over 55 days. The experiment was repeated three times, with independently derived transgenic lines. Similar results were obtained from each experiment. The experiment was carried out under red light (Kodak Safelight Filter 1A). Control flies were of the genotype *elav*–GAL4/+. Experimental animals were of the following genotypes: (1) *elav*–GAL4/+; *UAS–wild-type* α-*synuclein*/+; (2) *UAS–A30P* α-*synuclein*/*elav*–GAL4; and (3) *UAS–A53T* α-*synuclein*/*elav*–GAL4.

Received 14 February; accepted 2 March 2000.

1. Polymeropoulos, M. H. *et al.* Mutation in the α-synuclein gene identified in families with Parkinson's disease. *Science* **276,** 2045–2047 (1997).
2. Krüger, R. *et al.* Ala30Pro mutation in the gene encoding α-synuclein in Parkinson's disease. *Nature Genet.* **18,** 106–108 (1998).
3. Spillantini, M. G., Schmidt, M. L., Lee, V. M. -Y. & Trojanowski, J. Q. α-Synuclein in Lewy bodies. *Nature* **388,** 839–840 (1997).
4. Spillantini, M. G., Crowther, R. A., Jakes, R., Hasegawa, M. & Goedert, M. α-Synuclein in filamentous inclusions of Lewy bodies from Parkinson's disease and dementia with Lewy bodies. *Proc. Natl Acad. Sci. USA* **95,** 6469–6473 (1998).
5. Baba, M. *et al.* Aggregation of α-synuclein in Lewy bodies of sporadic Parkinson's disease and dementia with Lewy bodies. *Am. J. Pathol.* **152,** 879–884 (1998).
6. Brand, A. H. & Perrimon, N. Targeted gene expression as a means of altering cell fates and generating dominant phenotypes. *Development* **118,** 401–415 (1993).
7. Warrick, J. M. *et al.* Expanded polyglutamine protein forms nuclear inclusions and causes neural degeneration in *Drosophila*. *Cell* **93,** 939–949 (1998).
8. Budnik, V., Martin-Morris, L. & White, K. Perturbed pattern of catecholamine-containing neurons in mutant *Drosophila* deficient in the enzyme dopa decarboxylase. *J. Neurosci.* **6,** 3682–3691 (1986).
9. Budnik, V. & White, L. Catecholamine-containing neurons in *Drosophila melanogaster*: Distribution and development. *J. Comp. Neurol.* **268,** 400–413 (1988).
10. Lundell, M. J. & Hirsh, J. Temporal and spatial development of serotonin and dopamine neurons in the *Drosophila* CNS. *Dev. Biol.* **165,** 385–396 (1994).
11. Gibbs, W. R. G. & Lees, A. J. Anatomy, pigmentation, ventral and dorsal subpopulations of the substantia nigra, and differential cell death in Parkinson's disease. *J. Neurol. Neurosurg. Psychiatry* **54,** 388–396 (1991).
12. Coombe, P. E. & Heisenberg, M. The structural brain mutant *Vacuolar medulla* of *Drosophila melanogaster* with specific behavioral defects and cell degeneration in the adult. *J. Neurogenet.* **3,** 135–158 (1986).
13. Buchanan, R. L. & Benzer, S. Defective glia in the *Drosophila* brain degeneration mutant *drop-dead*. *Neuron* **10,** 839–850 (1993).
14. Jellinger, K. A. Pathology of Parkinson's disease. Changes other than the nigrostriatal pathway. *Mol. Chem. Neuropathol.* **14,** 153–197 (1991).
15. Vallés, A. M. & White, K. Serotonin-containing neurons in *Drosophila melanogaster*: Development and distribution. *J. Comp. Neurol.* **268,** 414–428 (1988).
16. Kuzuhara, S., Mori, H., Izumiyama, N., Yoshimura, M. & Ihara, Y. Lewy bodies are ubiquitinated: a light and electron microscopic immunocytochemical study. *Acta Neuropathol.* **75,** 345–353 (1988).
17. Dickson, D. W. *et al.* Diffuse Lewy body disease: light and electron microscopic immunocytochemistry of senile plaques. *Acta Neuropathol.* **78,** 572–584 (1987).
18. Pollanen, M. S., Dickson, D. W. & Bergeron, C. Pathology and biology of the Lewy body. *J. Neuropathol. Exp. Neurol.* **52,** 183–191 (1993).
19. Ganetzky, B. & Flanagan, J. R. On the relationship between senescence and age-related changes in two wild-type strains of *Drosophila melanogaster*. *Exp. Gerontol.* **13,** 189–196 (1978).
20. Le Bourg, E. & Lints, F. A. Hypergravity and aging in *Drosophila melanogaster*. 4. Climbing activity. *Gerontology* **38,** 59–64 (1992).
21. Franceschini, N. in *Information Processing in the Visual System of* Drosophila (ed. Wehner, R.) 75–82 (Springer, Berlin, 1972).
22. Conway, K. A., Harper, J. D. & Lansbury, P. T. Accelerated *in vitro* fibril formation by a mutant α-synuclein linked to early-onset Parkinson disease. *Nature Med.* **4,** 1318–1320 (1998).
23. Narhi, L. *et al.* Both familial Parkinson's disease mutations accelerate α-synuclein aggregation. *J. Biol. Chem.* **274,** 9843–9846 (1999).
24. El-Agnaf, O. M. A. *et al.* Aggregates from mutant and wild-type α-synuclein proteins and NAC peptide induce apoptotic cell death in human neuroblastoma cells by formation of β-sheet and amyloid-like filaments. *FEBS Lett.* **440,** 71–75 (1998).
25. Ostreova, N. *et al.* α-synuclein shares physical and functional homology with 14-3-3 proteins. *J. Neurosci.* **19,** 5782–5791 (1999).
26. Hong, L. *et al.* The cDNA cloning and ontogeny of mouse α-synuclein. *NeuroReport* **9,** 1239–1243 (1998).
27. Masliah, E. *et al.* Dopaminergic loss and inclusion body formation in α-synuclein mice: implications for neurodegenerative disorders. *Science* **287,** 1265–1269 (2000).
28. Li, H., Chaney, S., Forte, M. & Hirsh, J. Ectopic G-protein expression in dopamine and serotonin neurons blocks cocaine sensitization in *Drosophila melanogaster*. *Curr. Biol.* (in the press).
29. Robinow, S. & White, L. The locus *elav* of *Drosophila melanogaster* is expressed in all neurons at all developmental stages. *Dev. Biol.* **126,** 294–303 (1988).
30. Ellis M., O'Neill, E. & Rubin, G. Expression of *Drosophila* glass protein and evidence for negative regulation of its activity in non-neuronal cells by another DNA-binding protein. *Development* **119,** 855–865 (1993).

Acknowledgements

We thank J. Hirsh, J. Hardy, M. Farrer and H. Orr for flies and DNAs; J. Hirsh, D. Dickson, M. Frosch, K. Buckley, W. Quinn and D. Morisato for discussions; and H. Shing, L. Trakimas, A. Merola, C. Ridolfi and M. Ericsson for technical assistance. M.B.F. thanks J. Gusella and the American Parkinson Disease Foundation for encouragement. Support was provided by a Howard Hughes Physician Postdoctoral Fellowship and a grant from the N.I.A. to M.B.F, and by a grant from the N.I.H. to W.B.

Correspondence and requests for materials should be addressed to M.B.F. (e-mail: mel_feany@hms.harvard.edu).

Interleukin-1 polymorphisms associated with increased risk of gastric cancer

Emad M. El-Omar*†, Mary Carrington‡, Wong-Ho Chow*, Kenneth E. L. McColl§, Jay H. Bream‖, Howard A. Young‖, Jesus Herrera‡, Jolanta Lissowska¶, Chiu-Chin Yuan‡, Nathaniel Rothman*, George Lanyon§, Maureen Martin‡, Joseph F. Fraumeni Jr* & Charles S. Rabkin*

** Division of Cancer Epidemiology and Genetics, National Cancer Institute, Bethesda, Maryland, USA*
† Department of Medicine and Therapeutics, Aberdeen University, Aberdeen, UK
‡ Intramural Research Support Program, Science Applications International Corporation Frederick, National Cancer Institute-Frederick Cancer Research and Development Centre, Maryland, USA
§ Department of Medicine and Therapeutics, Western Infirmary, Glasgow, UK
‖ Division of Basic Sciences, National Cancer Institute, Frederick Cancer Research and Development Centre, Maryland, USA
¶ Division of Cancer Epidemiology and Prevention, Cancer Centre and M. Sklodowska-Curie Institute of Oncology, Warsaw, Poland

Helicobacter pylori **infection is associated with a variety of clinical outcomes including gastric cancer and duodenal ulcer disease[1]. The reasons for this variation are not clear, but the gastric physiological response is influenced by the severity and anatomical distribution of gastritis induced by *H. pylori*. Thus, individuals**

with gastritis predominantly localized to the antrum retain normal (or even high) acid secretion[2], whereas individuals with extensive corpus gastritis develop hypochlorhydria and gastric atrophy[3], which are presumptive precursors of gastric cancer[4]. Here we report that interleukin-1 gene cluster polymorphisms suspected of enhancing production of interleukin-1-beta are associated with an increased risk of both hypochlorhydria induced by *H. pylori* and gastric cancer. Two of these polymorphism are in near-complete linkage disequilibrium and one is a TATA-box polymorphism that markedly affects DNA–protein interactions *in vitro*. The association with disease may be explained by the biological properties of interleukin-1-beta, which is an important pro-inflammatory cytokine[5] and a powerful inhibitor of gastric acid secretion[6,7]. Host genetic factors that affect interleukin-1-beta may determine why some individuals infected with *H. pylori* develop gastric cancer while others do not.

H. pylori infects half of the world's population and has been implicated in the pathogenesis of gastric cancer[1], the second-most common malignancy worldwide[8]. The mechanism of *H. pylori*-induced carcinogenesis is not clear. The infection almost always causes inflammation of the gastric mucosa, the distribution and severity of which varies widely and affects the clinical outcome. Gastritis that is confined to the antral region is associated with excessive acid production and a high risk of duodenal ulcer disease[2]. In contrast, gastritis involving the acid-secreting corpus region leads to hypochlorhydria, progressive gastric atrophy[3] and an increased risk of gastric cancer[4,9]. These pre-cancerous changes are unfavourable to *H. pylori* growth and some gastric cancers arise long after the infection has disappeared. Duodenal ulceration and gastric cancer seem to be mutually exclusive outcomes of *H. pylori* infection that cannot be explained by differences in bacterial virulence factors alone, as virulent strains seem to be equally associated with both conditions[10,11]. An alternative explanation is that host genetic factors (in conjunction with bacterial and/or environmental factors) determine the immune and inflammatory responses to *H. pylori* infection. A critical factor in *H. pylori*-induced gastric carcinogenesis is gastric acid secretion, which both influences and is influenced by *H. pylori*-induced gastritis. If inflammation of the corpus mucosa is severe, acid secretion is inhibited and eventually lost through the destruction of gastric glands[3]. Furthermore, pharmacological inhibition of acid secretion leads to the re-distribution of *H. pylori*-induced gastritis with a reduced intensity of antral inflammation and an increased intensity in the corpus, and may progress to gastric atrophy in the long term[12]. Endogenous factors that suppress acid secretion could also contribute to corpus gastritis and atrophy.

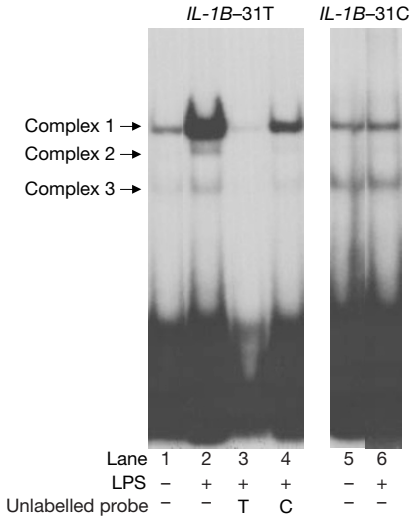

Figure 1 Differential binding patterns between the T- and C-bearing alleles of the *IL-1B* promoter. Nuclear extracts from fresh human monocytes stimulated for 30 min with lipopolysaccharide (LPS) (+) show evidence of induction of DNA–protein complexes 1 and 2 on the *IL-1B* − 31T oligonucleotide. Complex 3 and free probe were equivalent across all lanes. Cold competition with a 100-fold excess of unlabelled probe (T) blocked the formation of complex 1 (lane 3), whereas cross-competition with unlabelled *IL-1B* − 31C (C) only partially blocked complex 1 (lane 4). Results were similar with monocyte extracts from three different donors.

The interleukin-1 (*IL-1*) gene cluster on chromosome 2q contains 3 related genes within a 430-kilobase (kb) region, *IL-1A*, *IL-1B* and *IL-1RN*, which encode the pro-inflammatory cytokines IL-1α and IL-1β as well as their endogenous receptor antagonist IL-1ra respectively[5]. IL-1β is upregulated in the presence of *H. pylori* and is important in initiating and amplifying the inflammatory response to this infection[13–15]. IL-1β is also a potent inhibitor of gastric acid secretion[6,7]; on a molar basis it is estimated to be 100-fold more potent than proton pump inhibitors and 6,000-fold more potent

Table 1 Estimated haplotype frequencies and linkage disequilibrium coefficients

		Haplotype*						Disequilibrium†		
Population	Loci	1–1	1–2	2–1	2–2	1–3,4,5	2–3,4,5	*D′*	χ^2	*p*
GCR controls	*IL-1B* − 31/*IL-1B* − 511	0.610	0.010	0.005	0.375			0.98	95.2	0.0001
(*n* = 100)	*IL-1B* − 31/*IL-1B* + 3954	0.420	0.200	0.380	0.000			–0.53	27.8	0.0001
	IL-1B − 31/*IL-1RN*	0.519	0.096	0.131	0.244	0.005	0.005	0.52	26.6	0.0001
	IL − *1B* + 3954/*IL-1RN*	0.495	0.295	0.155	0.045	0.010	0.000	–0.20	3.8	0.05
Low acid GCR	*IL-1B* − 31/*IL-1B* − 511	0.422	0.000	0.022	0.556			0.96	41.4	0.0001
(*n* = 45)	*IL-1B* − 31/*IL-1B* + 3954	0.273	0.149	0.560	0.018			–0.27	3.3	0.07
	IL-1B − 31/*IL-1RN*	0.330	0.092	0.203	0.375	0.000	0.000	0.48	10.5	0.001
	IL − *1B* + 3954/*IL-1RN*	0.408	0.425	0.125	0.042	0.000	0.000	–0.17	1.4	0.24
Normal acid GCR	*IL-1B* − 31/*IL-1B* − 511	0.681	0.017	0.000	0.302			0.95	52.1	0.0001
(*n* = 58)	*IL-1B* − 31/*IL-1B* + 3954	0.527	0.171	0.275	0.027			–0.20	2.3	0.13
	IL-1B − 31/*IL-1RN*	0.611	0.087	0.130	0.155	0.000	0.017	0.47	12.6	0.0004
	IL − *1B* + 3954/*IL-1RN*	0.561	0.223	0.180	0.018	0.017	0.000	–0.25	3.6	0.06
Gastric cancer controls	*IL-1B* − 31/*IL-1B* − 511	0.699	0.002	0.000	0.298			1.00	426.6	0.0001
(*n* = 429)	*IL-1B* − 31/*IL-1B* + 3954	0.498	0.203	0.250	0.048			–0.16	11.2	0.0008
	IL-1B − 31/*IL-1RN*	0.612	0.084	0.109	0.185	0.005	0.004	0.51	112.6	0.0001
	IL − *1B* + 3954/*IL-1RN*	0.525	0.214	0.196	0.056	0.009	0.000	–0.07	2.1	0.14
Gastric cancer cases	*IL-1B* − 31/*IL-1B* − 511	0.576	0.008	0.003	0.413			0.98	352.4	0.0001
(*n* = 366)	*IL-1B* − 31/*IL-1B* + 3954	0.418	0.166	0.352	0.063			–0.19	12.8	0.0003
	IL-1B − 31/*IL-1RN*	0.423	0.155	0.152	0.259	0.007	0.004	0.39	54.7	0.0001
	IL − *1B* + 3954/*IL-1RN*	0.413	0.350	0.162	0.064	0.007	0.004	–0.17	11.0	0.0009

Data given for pairs of *IL-1* loci in gastric cancer relatives (GCR), gastric cancer cases and respective control populations.
* For all *IL-1B* loci, C is denoted by allele 1 and T is denoted by allele 2.
† $D' = D/D_{max}$ for association of most common alleles at each locus.

than H_2 antagonists[16]. Three diallelic polymorphisms in *IL-1B* have been reported, all representing C–T base transitions, at positions −511, −31 and +3954 base pairs (bp) from the transcriptional start site[17]. There are conflicting data regarding the functional effects of these polymorphisms on IL-1β production[18,19]. The *IL-1RN* gene has a penta-allelic 86-bp tandem repeat (VNTR) in intron 2, of which the less common allele 2 (*IL-1RN**2) is associated with a wide range of chronic inflammatory and autoimmune conditions[17]. *IL-1RN**2 is associated with enhanced IL-1β production *in vitro*[19], but data regarding its effects on IL-1ra production are contradictory[20–22].

To determine whether these polymorphisms are important with respect to the different outcomes of *H. pylori* infections, we studied their effects on gastric physiology in healthy subjects. We had previously shown that a cohort of 149 first-degree relatives of gastric cancer patients from the West of Scotland had a high prevalence of hypochlorhydria (defined as a pentagastrin-stimulated peak acid output of less than 15 mmol h^{-1}) in association with *H. pylori* infection[23]. Of the 103 (69%) gastric cancer relatives (GCR) infected with the *H. pylori*, 45 had hypochlorhydria and gastric atrophy and 58 had normal or high acid secretion. One hundred unselected newborns from the West of Scotland were available as population controls. We also had available a case-control study of gastric cancer, based on a population from Warsaw, Poland, in which there were 393 gastric cancer cases and 430 controls with DNA samples[24]. We were thus able to determine whether genotypes that modify IL-1β are associated with low acid secretion and gastric atrophy, and whether these same genotypes increase the risk of gastric cancer. These studies were reviewed and approved by the Institutional Review Boards and Ethics Committees of the US National Cancer Institute, the University of Glasgow Hospitals NHS Trust, and the M. Sklodowska-Curie Memorial Cancer Centre (Warsaw).

In both the Scottish and Polish control populations, the alleles at the individual loci of *IL-1B* and *IL-1RN* were in Hardy–Weinberg equilibrium, with non-significant χ^2 values. There was marked linkage disequilibrium among the loci within the gene cluster (see also ref. 25). Linkage disequilibrium between *IL-1B* − 31 and *IL-1B* − 511 was almost total, with 99.5% of the inferred haplotypes (*IL-1B* − 31/*IL-1B* − 511) in the combined control groups consisting of either T–T or C–C (Table 1). There was also strong linkage disequilibrium ($D' \approx 0.5$) between *IL-1B* − 31 and *IL-1RN* in both populations. However, the two groups differed with respect to linkage disequilibrium between *IL-1B* − 31 and *IL-1B* + 3954, which was strong in the Scottish population controls but relatively weak ($D' = -0.16$) in the Polish controls. There was no significant linkage disequilibrium between *IL-1B* + 3954 and *IL-1RN* in either control group.

There were no significant differences in genotype frequency for any *IL-1* marker between the GCR and controls or between the total *H. pylori*-infected and uninfected GCR (Table 2). Nevertheless, among the infected GCR, those with low acid secretion had a significantly higher frequency of the pro-inflammatory *IL-1RN**2 allele and the T–T haplotype of *IL-1B* − 31 and *IL-1B* − 511 (*IL-1B* − 31T/*1L-1B* − 511T), as compared with the GCR with normal or high acid secretion. Carriers of the T allele of *IL-1B* − 31 (*IL-1B* − 31T+) had an age-adjusted odds ratio of 9.1 (95% confidence interval (CI), 2.2–37), and there was little difference between the homozygous and heterozygous carriers (Table 2). *IL-1RN**2 homozygotes (*IL-1RN**2/*2) were also at increased risk of hypochlorhydria, although risk among the *IL-1RN**2 heterozygotes was not significantly increased (Table 2). In a logistic regression model including both factors, the estimated age-adjusted odds ratios for *IL-1B* − 31T+ and *IL-1RN**2/*2 were 7.5 (95% CI, 1.8–31) and 2.1 (95% CI, 0.7–6.3), respectively. The *IL-1B* + 3954 genotype was not associated with the risk of hypochlorhydria.

There were similar associations between these alleles and the risk of gastric cancer. Carriers of *IL-1B* − 31T had an increased gastric cancer risk at an odds ratio of 1.9 (95% CI, 1.5–2.6), with no significant difference between homozygotes and heterozygotes (Table 3). Moreover, *IL-1RN**2 was associated with an increased risk in homozygotes but not in heterozygotes (Table 3). In a logistic regression model including both of these genotypes, the estimated odds ratios for *IL-1B* − 31T+ and *IL-1RN**2/*2 were 1.6 (95% CI, 1.2–2.2) and 2.9 (95% CI, 1.9–4.4), respectively. *IL-1B* + 3954T homozygotes seemed to be protected against gastric cancer, although the effect did not reach statistical significance (Table 3).

The estimated effects of *IL-1B* − 31T+ and *IL-1RN**2/*2 were similar in subgroups of gastric cancer cases defined by age, sex, histological type and anatomical site (data not shown). Furthermore, adjustment for other reported risk factors for gastric cancer, including tobacco and alcohol use, ABO blood group and family history of gastric cancer, did not substantially alter the estimates (data not shown).

The *IL-1B* − 31T/*IL-1RN**2 haplotype imparted a greatly increased risk of gastric cancer, as compared with having no copy of *IL-1B* − 31T and at least one copy of the other *IL-1RN* alleles. Twenty-two per cent of cases (compared with eight per cent of controls) had this haplotype, either in its homozygous form or with *IL-1B* − 31C/*IL-1RN**2, with an odds ratio of 4.4 (95% CI, 2.8–6.9). In the absence of *IL-1B* − 31T, homozygous *IL-1RN**2 was associated with a similarly elevated odds ratio of 5.3 (95% CI, 1.9–14), although this genotype combination was uncommon because of linkage disequilibrium between the two loci. In contrast, the odds ratio for *IL-1B* − 31T+ with no more than one copy of *IL-1RN**2 was only 1.7 (95% CI, 1.2–2.3). Nonetheless, because its effect is observed in both homozygotes and heterozygotes, the *IL-1B* − 31T allele accounts for a greater proportion of excess gastric cancer cases than the *IL-1RN**2 allele, despite their comparable frequencies. The

Table 2 *IL-1* genotype frequencies in gastric cancer relatives (GCR) and controls

		H. pylori-infected GCR				
Locus	Genotype	Low acid ($n = 45$)	Normal acid ($n = 58$)	Odds ratio (95% CI)*	Uninvected GCR ($n = 46$)	Population controls ($n = 100$)
IL-1B − 31	C/C	5	30	1.0	23	37
	C/T	28	21	8.1 (2.0–33)	18	50
	T/T	12	7	13.6 (2.6–71)	5	13
IL-1B − 511	C/C	5	29	1.0	23	36
	C/T	30	21	8.3 (2.0–34)	18	51
	T/T	10	8	11.4 (2.2–58)	5	13
IL-1B + 3954	C/C	30	35	1.0	28	67
	C/T	15	23	0.8 (0.3–1.9)	15	26
	T/T	0	0		3	7
IL-1RN	1/1	17	35	1.0	24	42
	1/2	14	14	2.4 (0.9–6.2)	15	44
	1/3, 4, 5	0	2	0	0	2
	2/2	14	7	5.6 (1.8–17)	7	12

*Odds ratio for low acid versus normal/high acid, adjusted for age and within-family sampling. CI, confidence interval.

fraction of gastric cancer in the population that is attributable to *IL-1B* − 31T is estimated to be 31%, compared with 18% for *IL-1RN**2. Their combined population attributable fraction is estimated to be 38%, which represents the fraction of gastric cancer cases that are caused by these *IL-1* alleles.

The *IL-1B* − 31 polymorphism involves a TATA sequence in the *IL-1B* promoter. To investigate the effect of *IL-1B* − 31 variants on the induction of IL-1β, we used electrophoretic mobility-shift analysis to assess their DNA-binding activity *in vitro*. Synthetic allele-specific oligonucleotides representing the polymorphic *IL-1B* − 31 sites were incubated with nuclear protein extracts from non-stimulated human monocytes and monocytes activated by lipopolysaccharide (LPS). LPS stimulation induced a fivefold increase in DNA binding (complex 1) on the *IL-1B* − 31T oligonucleotide (Fig. 1, lanes 1 and 2). In contrast, LPS failed to induce complex 1 formation on the *IL-1B* − 31C oligonucleotide (Fig. 1, lanes 5 and 6). Furthermore, complex 1 formation on radiolabelled *IL-1B* − 31T was specifically blocked by competition with the unlabelled *IL-1B* − 31T, but not the *IL-1B* − 31C, oligonucleotide (Fig. 1, lanes 3 and 4). These results indicate that one or more proteins (presumably transcription factors) in complex 1 may be unable to interact with the C-bearing *IL-1B* − 31 allele to form the transcription initiation complex. In parallel experiments assessing allele-specific oligonucleotides for *IL-1B* − 511, there were no differences in binding activity (data not shown), indicating that the effect of *IL-1B* − 511 may be mediated by linkage disequilibrium with the TATA box polymorphism. On the basis of these results and previously published functional data for *IL-1RN*, hypochlorhydria and gastric cancer may be associated with alleles of *IL-1B* − 31 and *IL-1RN* that enhance IL-1β production.

Here we demonstrate that pro-inflammatory genotypes of the *IL-1* loci (*IL-1B* − 31T+ and *IL-1RN**2/*2) increase both the likelihood of a chronic hypochlorhydric response to *H. pylori* infection and the risk of gastric cancer, presumably by altering IL-1β levels in the stomach. While the pro-inflammatory effects of high IL-1β concentrations may facilitate the clearance of *H. pylori* from the gastric mucosa, the concomitant inhibition of acid secretion allows the spread of *H. pylori*-induced inflammation from the antrum to the corpus. This functional inhibition is initially reversible but the progressive destruction of parietal cells eventually leads to irreversible hypochlorhydria. A decreased flow of gastric secretions may therefore heighten mucosal damage by allowing the accumulation of bacterial toxins and by-products of inflammation that would normally be diluted and flushed out. The reactive oxygen and nitrogen oxide species that are derived from inflammation are known mutagens, while hypochlorhydria permits superinfection by other bacteria that enhance the production of highly carcinogenic *N*-nitroso compounds[26].

H. pylori-induced hypochlorhydria also markedly reduces the levels of vitamin C in gastric juice[27], further facilitating the formation of *N*-nitroso compounds. The opportunities for DNA damage caused by this cascade of genotoxic factors are amplified by the increased rate of cell turnover in inflamed mucosa. Therefore, genotypes that enhance IL-1β production may favour the initiation of a set of responses to *H. pylori* that result in hypochlorhydria, corpus atrophy and an increased risk of gastric cancer.

Our findings complement the most widely accepted multi-stage model of gastric carcinogenesis[4], and provide insights into the etiological role of *H. pylori*. We have shown at least two susceptibility loci in the *IL-1* gene cluster for gastric cancer and its precursors. The effects of these loci influence an early stage of the disease process and require the presence of *H. pylori* infection. Progression towards cancer is probably influenced by other components of the host genetic constitution acting epistatically, as well as by dietary and other factors in the environment. *IL-1B* − 31T/*IL-1RN**2 constitutes a pro-inflammatory haplotype that is in strong linkage disequilibrium, at least in Caucasian populations. We speculate that this linkage disequilibrium reflects past selective pressures for or against enhancement of the IL-1β response to environmental challenges. Whereas pro-inflammatory genotypes may be advantageous for the host response to some infections, the vigorous IL-1β production associated with *H. pylori* gastric infection may exacerbate mucosal damage and increase the risk of eventual neoplasia. □

Table 3 *IL-1* genotype frequencies in gastric cancer cases and controls

Locus	Genotype	Cases (n = 366)	Controls (n = 429)	Odds ratio (95% CI)
IL-1B − 31	C/C	128	219	1.0
	C/T	172	164	1.8 (1.3–2.4)
	T/T	66	46	2.5 (1.6–3.8)
IL-1B − 511	C/C	127	217	1.0
	C/T	170	166	1.8 (1.3–2.4)
	T/T	69	46	2.6 (1.7–3.9)
IL-1B + 3954	C/C	212	242	1.0
	C/T	140	158	1.0 (0.8–1.4)
	T/T	14	29	0.6 (0.3–1.1)
IL-1RN	1/1	148	230	1.0
	1/2	117	152	1.2 (0.9–1.6)
	1/3, 4, 5	8	7	1.8 (0.7–4.8)
	2/2	93	39	3.7 (2.4–5.7)
	2/5	0	1	0

Methods

IL-1 genotyping

IL-1B polymorphisms were distinguished by two separate methods, polymerase chain reaction single-strand conformation polymorphism (PCR-SSCP) and 5′ nuclease PCR assays (TaqMan). For PCR-SSCP, 50 ng DNA was amplified in a GeneAmp PCR System 9700 (PE Applied Biosystems), using the primer pairs listed in the Supplementary Information. Amplification was performed in a volume of 20 μl, containing 10 mM Tris-HCl pH 8.3, 50 mM KCl, 1.5 mM $MgCl_2$, 200 μM each of dATP, dTTP and dGTP, 100 μM dCTP, 1 μCi of [α-^{32}P]dCTP (3,000 Ci mol^{-1}), 80 ng of each primer and 1 unit of Taq polymerase. The thermocycling conditions were as follows: 94 °C for 10 min; then 5 cycles of 94 °C for 30 s, 65 °C for 30 s and 72 °C for 30 s; then 30 cycles of 94 °C for 30 s, 60 °C for 30 s and 72 °C for 30 s; then 5 cycles of 94 °C for 30 s, 55 °C for 30 s and 72 °C for 30 s. SSCP analysis of the radiolabelled amplification products was performed as described[28].

For TaqMan assays, primers (Operon Technologies Inc.) and probes (PE Applied Biosystems) were designed using Primer Express software (PE Applied Biosystems). Probes for the T or C allele were 5′-labelled with either FAM (6-carboxyfluoresceine) or VIC fluorogenic dyes, and 3′-labelled with TAMRA (6-carboxytetramethylrhodamine) quencher. PCR amplification was performed in a volume of 25 μl containing 50 ng genomic DNA, 1× TaqMan Universal Master Mix (PE Applied Biosystems), 200 nM for each probe and 900 nM for primers. Cycling conditions were 50 °C for 2 min, 95 °C for 10 min, then 40 cycles of 95 °C for 15 s and 62 °C for 1 min, as recommended by the manufacturer. Thermal cycling of optical plates was performed in GeneAmp PCR System 9700 and endpoint analysis was performed in the ABI PRISM 7700 Sequence Detection System (PE Applied Biosystems). Sequences of primers and probes for *IL-1B* TaqMan assays are available from the authors.

For *IL-1RN*, genomic DNA was amplified using PCR under the conditions described above for *IL-1B*, using forward primer 5′-CCCCTCAGCAACACTCC-3′ and reverse primer 5′-GGTCAGAAGGGCAGAGA-3′. The PCR products were separated by electrophoresis on 2% agarose gels and stained with ethidium bromide. Alleles were sized relative to a 1-kb DNA ladder and coded conventionally as follows: allele 1 = 4 repeats, allele 2 = 2 repeats, allele 3 = 5 repeats, allele 4 = 3 repeats, allele 5 = 6 repeats; the rarer alleles 3, 4 and 5 were grouped in the statistical analysis.

A total of 93% (366/393) of the gastric cancer cases, 99% (429/430) of their population controls, and all GCR subjects and their newborn population controls were successfully genotyped for all four loci.

Electrophoretic mobility shift assay (EMSA)

Nuclear extracts were prepared from freshly isolated human monocytes as described[29], after no stimulation or addition of 1 μg ml^{-1} LPS derived from *E. coli* (Sigma) for 30 min. Complementary single-stranded oligonucleotides were synthesized (Life Technologies) as follows (variant nucleotides in bold):

IL-1B − 31 : 5′-TGCTTTTGAAAGC**C/T**ATAAAAACAGCG-3′

IL-1B − 511 : 5′-TGACAGAGAGCTCC**C/T**GAGGCAGAGAAC-3′

Complementary strands were annealed by combining 2 μg of each oligonucleotide and 6 μl of 10× annealing buffer (500 mM Tris, 100 mM $MgCl_2$ and 50 mM dithiothreitol) in a 60-μl reaction, placing in a boiling water bath for 5 min and allowing to cool to room temperature. The DNA–protein binding reaction was conducted in a 20-μl volume containing 7 μg of nuclear protein extract, 1 μg poly (dI–dC) (Sigma), 4 μl of 5× binding

buffer (60 mM HEPES, 7.5 mM $MgCl_2$, 300 mM KCl, 1 mM ethylenediamine-tetraacetic acid, 2.5 mM dithriothreitol, 50% glycerol and 4-(2-aminoethyl)-benzenesulphonyl fluoride hydrochloride) and 2.5×10^4 c.p.m. of ^{32}P-labelled oligonucleotide probe. UN-SCAN-IT 5.1 software (Silk Scientific) was used for densitometric analysis of the autoradiographs.

Statistical analysis

Hardy–Weinberg equilibrium of alleles at individual loci was assessed by χ^2 statistics. Haplotype frequencies for pairs of alleles were estimated using the Estimating Haplotype-frequencies (EH) software program (ftp://linkage.rockefeller.edu/software/eh). Linkage disequilibrium coefficients $D' = D/D_{max}$ and χ^2 values were calculated for pairs of the most common alleles at each locus using the LINKDOS software program (distributed with GENEPOP, ftp://ftp.cefe.cnrs-mop.fr/pub/PC/MSDOS/GENEPOP/). Odds radios with Cornfield 95% confidence intervals and logistic regression models controlling for the effects of possible confounders were computed using STATA version 5.0 software (STATA Press). The odds ratios for hypochlorhydria were age-adjusted (categorized as ⩽35, 36–45, 46–55 and >55 years) because of its age-dependence[23] and their confidence intervals were based on robust variance estimates[30] which adjust for within-family correlation, to account for sampling of several members of a given family.

Received 21 October 1999; accepted 4 February 2000.

1. Blaser, M. J. *Helicobacter pylori* and gastric diseases. *Br. Med. J.* **316**, 1507–1510 (1998).
2. El-Omar, E. *et al. Helicobacter pylori* infection and abnormalities of acid secretion in patients with duodenal ulcer disease. *Gastroenterology* **109,** 681–691 (1995).
3. El-Omar, E. *et al. Helicobacter pylori* infectin and chronic gastric acid hyposecretion. *Gastroenterology* **113,** 15–24 (1997).
4. Correa, P. Human gastric carcinogenesis: a multistep and multifactorial process—First American Cancer Society Award Lecture on Cancer Epidemiology and Prevention. *Cancer Res.* **52,** 6735–6740 (1992).
5. Dinarello, C. A. Biologic basis for interleukin-1 in disease. *Blood* **87,** 2095–2147 (1996).
6. Wallace, J. L., Cucala, M., Mugridge, K. & Parente, L. Secretagogue-specific effects of interleukin-1 on gastric acid secretion. *Am. J. Physiol.* **261,** G559–G564 (1991).
7. Beales, I. L. & Calam, J. Interleukin 1 beta and tumour necrosis factor alpha inhibit acid secretion in cultured rabbit parietal cells by multiple pathways. *Gut* **42,** 227–234 (1998).
8. Parkin, D. M., Pisani, P. & Ferlay, J. Estimates of the worldwide incidence of 25 major cancers in 1990. *Int. J. Cancer* **80,** 827–841 (1999).
9. Sipponen, P. Gastric cancer—a long-term consequence of Helicobactor pylori infection? *Scand. J. Gastroenterol.* **201,** (suppl.), 24–27 (1994).
10. Yamaoka, Y. *et al.* Relationship between *Helicobacter pylori* iceA, cagA, and vacA status and clinical outcome: studies in four different countries. *J. Clin. Microbiol.* **37,** 2274–2279 (1999).
11. Hansson, L. E. *et al.* The risk of stomach cancer in patients with gastric or duodenal ulcer disease. *N. Engl. J. Med.* **335,** 242–249 (1996).
12. Kuipers, E. J. *et al.* Atrophic gastritis and *Helicobacter pylori* infection in patients with reflux esophagitis treated with omeprazole or fundoplication. *N. Engl. J. Med.* **334,** 1018–1022 (1996).
13. Noach, L. A. *et al.* Mucosal tumor necrosis factor-alpha, interleukin-1 beta, and interleukin-8 production in patients with *Helicobacter pylori* infection. *Scand. J. Gastroenterol.* **29,** 425–429 (1994).
14. Basso, D. *et al. Helicobacter pylori* infection enhances mucosal interleukin-1 beta, interleukin-6, and the soluble receptor of interleukin-2. *Int. J. Clin. Lab. Res.* **26,** 207–210 (1996).
15. Jung, H. C., Kim, J. M., Song, I. S. & Kim, C. Y. *Helicobacter pylori* induces an array of pro-inflammatory cytokines in human gastric epithelial cells: quantification of mRNA for interleukin-8, -1 alpha/beta, granulocyte-macrophage colony-stimulating factor, monocyte chemoattractant protein-1 and tumour necrosis factor-alpha. *J. Gastroenterol. Hepatol.* **12,** 473–480 (1997).
16. Wolfe, M. M. & Nompleggi, D. J. Cytokine inhibition of gastric acid secretion—a little goes a long way. *Gastroenterology* **102,** 2177–2178 (1992).
17. Bidwell, J. L. *et al.* Cytokine gene polymorphism in human disease: on-line databases. ⟨http://www.pam.bris.ac.uk/services/GAI/cytokine4.htm.⟩
18. Pociot, F. *et al.* A TaqI polymorphisms in the human interleukin-1 beta (IL-1 beta) gene correlates with IL-1 beta secretion in vitro. *Eur. J. Clin. Invest.* **22,** 396–402 (1992).
19. Santtila, S., Savinainen, K. & Hurme, M. Presence of the IL-1RA allele 2 (IL1RN*2) is associated with enhanced IL-1beta production in vitro. *Scand. J. Immunol.* **47,** 195–198 (1998).
20. Andus, T. *et al.* Imbalance of the interleukin 1 system in colonic mucosa—association with intestinal inflammation and interleukin 1 receptor antagonist genotype 2. *Gut* **41,** 651–657 (1997).
21. Danis, V. A., Millington, M., Hyland, V. J. & Grennan, D. Cytokine production by normal human monocytes: inter-subject variation and relationship to an IL-1 receptor antagonist (IL-1Ra) gene polymorphism. *Clin. Exp. Immunol.* **99,** 303–310 (1995).
22. Tountas, N. A. *et al.* Functional and ethnic association of allele 2 of the interleukin-1 receptor antagonist gene in ulcerative colitis. *Gastroenterology* **117,** 806–813 (1999).
23. El-Omar, E. M. *et al.* Increased prevalence of precancerous changes in relatives of gastric cancer patients: critical role of *H. pylori*. *Gastroenterology* **118,** 22–30 (2000).
24. Chow, H. W. *et al.* Risk of stomach cancer in relation to consumption of cigarettes, alcohol, tea and coffee in Warsaw, Poland. *Int. J. Cancer* **81,** 871–876 (1999).
25. Cox, A., Camp, N. J., Nicklin, M. J., Di Giovine, F. S. & Duff, G. W. An analysis of linkage disequilibrium in the interleukin-1 gene cluster, using a novel grouping method for multiallelic markers. *Am. J. Hum. Genet.* **62,** 1180–1188 (1998).
26. Stockbruegger, R. W. *et al.* Pernicious anaemia, intragastric bacterial overgrowth, and possible consequences. *Scand. J. Gastroenterol.* **19,** 355–364 (1984).
27. Ruiz, B. *et al.* Vitamin C concentration in gastric juice before and after anti-*Helicobacter pylori* treatment. *Am. J. Gastroenterol.* **89,** 533–539 (1994).
28. Carrington, M. *et al.* Typing of HLA-DQA1 and DQB1 using DNA single-strand conformation polymorphism. *Hum. Immunol.* **33,** 208–212 (1992).
29. Yu, C. R. *et al.* Differential utilization of Janus kinase-signal transducer activator of transcription signaling pathways in the stimulation of human natural killer cells by IL-2, IL-12, and IFN-alpha. *J. Immunol.* **157,** 126–137 (1996).
30. Royall, R. M. Model robust confidence intervals using maximum likelihood estimators. *Int. Stat. Rev.* **54,** 221–226 (1986).

Supplementary information is available on *Nature*'s World-Wide Web site (http://www.nature.com) or as paper copy from the London editorial office of *Nature*.

Acknowledgements

We thank A. Goldstein and N. Chatterjee for advice on genetic and statistical issues, N. Dunlap for technical assistance, D. Gillen for help with subject recruitment and J. Goedert for suggestions. E.M.E. received a European *Helicobacter pylori* Study Group Research Fellowship from the Digestive Disorders Foundation, UK. This project was partly funded by the National Cancer Institute, National Institutes of Health, USA.

Correspondence and requests for materials should be addressed to E.M.E. (e-mail: elomare@mail.nih.gov).

PKC-θ is required for TCR-induced NF-κB activation in mature but not immature T lymphocytes

Zuoming Sun*, Christopher W. Arendt*, Wilfried Ellmeier*†, Edward M. Schaeffer‡§, Mary Jean Sunshine*†, Leena Gandhi*, Justin Annes*, Daniela Petrzilka*†, Abraham Kupfer‖, Pamela L. Schwartzberg‡ & Dan R. Littman*†

† *Howard Hughes Medical Institute and * Molecular Pathogenesis Program, Skirball Institute of Biomolecular Medicine, New York University School of Medicine, New York, New York 10016, USA*
‡ *National Human Genome Research Institute, National Institutes of Health, Bethesda, Maryland 20892, USA*
§ *Department of Pathology, University of Chicago, Chicago, Illinois 60637, USA*
‖ *Division of Basic Science, Department of Pediatrics, National Jewish Medical and Research Center, Denver, Colorado 80262, USA*

Productive interaction of a T lymphocyte with an antigen-presenting cell results in the clustering of the T-cell antigen receptor (TCR) and the recruitment of a large signalling complex to the site of cell–cell contact[1,2]. Subsequent signal transduction resulting in cytokine gene expression requires the activation of one or more of the multiple isoenzymes of serine/threonine-specific protein kinase C (PKC)[3]. Among the several PKC isoenzymes expressed in T cells, PKC-θ is unique in being rapidly recruited to the site of TCR clustering[4]. Here we show that PKC-θ is essential for TCR-mediated T-cell activation, but is dispensable during TCR-dependent thymocyte development. TCR-initiated NF-κB activation was absent from *PKC-θ*$^{-/-}$ mature T lymphocytes, but was intact in thymocytes. Activation of NF-κB by tumour-necrosis factor α and interleukin-1 was unaffected in the mutant mice. Although studies in T-cell lines had suggested that PKC-θ regulates activation of the JNK signalling pathway[5,6], induction of JNK was normal in T cells from mutant mice. These results indicate that PKC-θ functions in a unique pathway that links the TCR signalling complex to the activation of NF-κB in mature T lymphocytes.

We inactivated the gene encoding PKC-θ by homologous recombination in embryonic stem cells by replacing the exon encoding the ATP-binding site of the kinase domain (amino-acid residues 396–451) with the *neomycin* resistance gene. Homozygous mutant mice seemed normal and were fertile. Immunoblot analysis with antibodies directed against sequences outside the deleted coding region of PKC-θ failed to detect any protein product, even of smaller than normal size, in thymocytes or T cells from the mutant animals (data not shown). Flow cytometric analyses of cells from thymus, spleen and lymph nodes of the mutant mice were indistinguishable from